Unlocking d-Orbital Tunability in Nickel-Based Hydroxide by High-Entropy Strategy for Boosting Electrocatalytic 5-Hydroxymethylfurfural Oxidation

Zhilong Yu[a], Hairui Guo[a], Huanhuan Zhang[a], Huiling Liu [a,*], Peilei He [b,*] and Cheng Wang[a]

[a]*Institute for New Energy Materials and Low-Carbon Technologies, School of Materials Science and Engineering, Tianjin Key Laboratory of Advanced Functional Porous Materials, Tianjin University of Technology, Tianjin, 300384, China. E-mail: hlliu_tjut2016@163.com*

[b]*School of Materials Science and Engineering, Tianjin University of Technology, Tianjin, 300384, China. E-mail: hepeilei@email.tjut.edu.cn*

Chemicals and materials

All the chemicals were obtained from commercial sources and used as received without further purification unless otherwise stated. Cobalt nitrate hexahydrate ($Co(NO_3)_2·6H_2O$, 99%, Aladdin Industrial Corporation), nickel nitrate hexahydrate ($Ni(NO_3)_2·6H_2O$, 99%, Aladdin Industrial Corporation), copper nitrate trihydrate ($Cu(NO_3)_2·3H_2O$, 99%, Aladdin Industrial Corporation), cadmium nitrate tetrahydrate ($Cr(NO_3)_2·9H_2O$, 99%, Macklin Biochemical Technology Co., Ltd), manganese nitrate solution ($Mn(NO_3)_2$, 50 wt.% in H_2O, Aladdin Industrial Corporation), urea (CH_4N_2O, 99%, Aladdin Industrial Corporation), ammonium fluoride (NH_4F, 99%, Sinopharm Chemical Reagent Co., Ltd), 5-hydroxymethyl-2-furaldehyde (HMF, $C_6H_6O_3$, 95%, Macklin Biochemical Technology Co., Ltd.), 5-hydroxymethyl-2-furancarboxylic acid (HMFCA, $C_6H_6O_4$, 98%, Aladdin Industrial Corporation), 2,5-diformylfuran (DFF, $C_6H_5O_3$, 98%, Aladdin Industrial Corporation), 5-formyl-2-furancarboxylic acid (FFCA, $C_6H_5O_4$, 98%, Aladdin Industrial Corporation), 2,5-furandicarboxylic acid (FDCA, $C_6H_4O_5$, 98%, Aladdin Industrial Corporation), potassium hydroxide (KOH, 90 %, Aladdin Industrial Corporation), ammonium formate (99%, Aladdin Industrial Corporation), methanol (CH_3OH, 99%, Tianjin Kemiou Chemical Reagent Co., Ltd),

ethanol (C_2H_5OH, 99%, Tianjin Kemiou Chemical Reagent Co., Ltd), Pt/C catalysts (Ron Chemical Co., Limited) were used. Ultrapure water with resistivity of 18.25 MΩ cm^{-1} was used throughout the experiments.

Nickel foam pretreatment

Nickel foam (NF) was used as the substrate, with a size of 1 cm × 3 cm. It was ultrasonically cleaned in a 3 M HCl solution for 30 minutes to remove the surface oxide layer. Then, the NF was successively transferred to ethanol and water for ultrasonic cleaning (10 minutes each time). Finally, it was dried at 60 ℃ to obtain clean NF.

Synthesis of LHs

Nickel foam (NF) was used as the substrate, with a size of 1 cm × 3 cm. It was ultrasonically cleaned in a 3 M HCl solution for 30 minutes to remove the surface oxide layer. Then, the NF was successively transferred to ethanol and water for ultrasonic cleaning (10 minutes each time). Finally, it was dried at 60 ℃ to obtain clean NF. Subsequently, HE-LHs sample was prepared via a one-step hydrothermal method. Briefly, 0.9 mmol of $Ni(NO_3)_2·6H_2O$, 0.2 mmol of $Cr(NO_3)_3·9H_2O$, 0.1 mmol of $Co(NO_3)_2·6H_2O$, 0.1 mmol of $Cu(NO_3)_2·3H_2O$, and 0.1 mmol of $Mn(NO_3)_2$ was dissolved in 30 mL of water. Subsequently, 9 mmol of urea and 3.5 mmol of NH_4F were added, and the mixture was stirred continuously for 1 h. The resulting clear solution was transferred into a 100 mL Teflon-lined stainless-steel autoclave along with a piece of pretreated NF, and then heated at 120 ℃ for 12 h in an oven. After naturally cooling to room temperature, the obtained sample was washed several times with water and ethanol, and dried in a vacuum oven at 60 °C for 12 h. For comparison, NiCoMnCr-LHs and NiCoMn-LHs samples were synthesized using the same procedure with corresponding metal precursors.

Characterization

The crystallographic characteristics of the samples were characterized by X-ray diffraction (XRD) on a SmartLab 9 kW (Rigaku, Japan), employing Cu Kα X-rays (λ = 0.l54598 nm) and

an acceleration voltage of 40 kV. The morphology of the obtained catalysts was observed by scanning electron microscopy (SEM, Quanta FEG 250, USA) and transmission electron microscopy (TEM, Talos F200 X, USA). The chemical composition and valence state of the samples were investigated by X-ray photo electron spectroscopy (XPS) using an ESCALAB250Xi spectrometer (Thermo Scientific, UK) with an Al-Kα radiation source under an acceleration voltage of 15 kV. The binding energies of the elements were calibrated against the C 1s peak at 284.8 eV. Inductively coupled plasma mass spectrometry (ICP-MS) analysis was performed on a Thermo Fisher Scientific iCAP RQ (Thermo Fisher Scientific, Germany) to determine the elemental composition and metal ratios in the synthesized HE-LHs. ^{1}H NMR spectra were recorded on a 400 MHz Bruker Avance III HD (Bruker Corporation, Switzerland) spectrometer to confirm the chemical structure and purity of the FDCA product. FTIR spectra were collected using a Perkin Elmer Spectrum Two spectrometer (Perkin Elmer, USA) in ATR mode to identify the functional groups and verify the successful conversion from HMF to FDCA. The Raman spectra of the samples were captured using a HORIBA EVOLUTION laser Raman spectrometer (France) with a 532 nm He/Ne laser as the excitation source, and the scanning range was set from 100 to 1000 cm^{-1}.

Electrochemical measurements

All of the static electrochemical measurements were performed using a three-electrode system in an H-type cell (10 mL) separated by a Nafion 117 proton exchange membrane. Unless otherwise stated, all static electrochemical tests were conducted using a Metrohm Autolab PGSTAT302N electrochemical workstation. Catalyst-loaded NF with a geometric area of 1 cm × 1 cm was used as the working electrode, and a graphite rod and a Hg/HgO electrode served as the counter electrode and reference electrode, respectively. Measurements were carried out at room temperature in 1 M KOH containing 50 mM HMF for hydroxymethylfurfural oxidation reaction (HMFOR). All potentials were converted to the reversible hydrogen electrode (RHE) scale using the following equation:

$$E_{vs.\,RHE} = E_{vs.\,Hg/HgO} + 0.098 + 0.059 \times pH \quad (1)$$

Cyclic voltammetry (CV) was conducted at a scan rate of 100 mV s^{-1}. Linear sweep

voltammetry (LSV) for HMFOR was performed at 5 mV s^{-1}. Constant potential electrolysis was carried out at applied potentials of 1.325, 1.375, 1.425, 1.475, 1.525, and 1.575 V vs. RHE. Electrochemical impedance spectroscopy (EIS) was measured in situ over a frequency range from 10^{-2} to 10^{5} Hz. The electrochemical surface area (ECSA) was estimated from the double-layer capacitance (C_{dl}), determined by recording CV at various scan rates (20, 40, 60, 80, and 100 mV s^{-1}) in a non-Faradaic potential region (1.02-1.12 V vs. RHE). The charging current was plotted against scan rate, and the slope of the linear fit corresponds to C_{dl} the ECSA of catalyst was calculated by dividing the C_{dl} to the specific capacitance (C_s = 0.04 mF/cm^2).

In the continuous HMFOR-HER and OER-HER systems, LSV and stability tests were performed using a two-electrode configuration, with HE LDH@NF as the anode and Pt/C@NF as the cathode, in a flow-mode electrolyzer containing 1 M KOH electrolyte with 100 mM HMF (30 mL) or in pure 1 M KOH (30 mL). Stability was evaluated by constant-current electrolysis at 150 mA cm^{-2}.

Product analysis

Product analysis was performed using high-performance liquid chromatography (HPLC, Shimadzu Prominence LC-2030C system) equipped with an ultraviolet-visible detector. A Shimpack GWS C18 column (5 μm, 4.6 × 150 mm) was employed for the separation of HMF, reaction intermediates (including HMFCA, FFCA, and DFF), and the final oxidation product (FDCA). During potentiostatic electrolysis, 4 μL of electrolyte was collected at designated intervals, diluted with ultrapure water to a total volume of 1 mL, and analyzed by HPLC. The UV detection wavelength was set to 265 nm. The mobile phase consisted of methanol (phase A) and a 5 mM ammonium formate aqueous solution (phase B), with a volume ratio A:B of 2.5:7.5, delivered at a flow rate of 0.5 mL min^{-1}. The column temperature was maintained at 45 °C, and each analytical run was completed within 11 min. The HMF conversion, FDCA yield, faradaic efficiency (FE), and yield rate were calculated according to the following equations:

$$HMF\ conversion\ (\%) = \frac{mol\ of\ HMF\ consumed}{mol\ of\ HMF\ initial} \times 100\% \quad (2)$$

$$FDCA\ yield\ (\%) = \frac{mol\ of\ FDCA\ formed}{mol\ of\ HMF\ consumed} \times 100\% \quad (3)$$

$$FE\ (\%) = \frac{mol\ or\ FDCA\ formed}{(Q\ /\ (6 \times F)\ )} \times 100\% \quad (4)$$

$$FDCA\ yield\ rate = \frac{mol\ of\ FDCA\ \times 1000}{S \times\ t} \quad (5)$$

The mol of HMF and FDCA is measured by HPLC. The Q is the total charge for the electrolysis, the F represents the Faraday constant (96485 C mol^{-1}), the S is the electrode geometric area, and t is the electrolysis time (h).

Multi-potential step (STEP) tests

Multi-potential step (STEP) tests were performed to monitor current responses under pulsed potentials. The potential was held at a high value (E_h = 1.475 V vs. RHE) for 4 s, then switched to a low potential (E_l) and maintained for 10 s, before returning to E_h for another 4 s. This cycle was repeated while incrementally raising E_h from 1.475 V to 1.575 V vs. RHE in steps of 20 mV, with E_l kept constant. The charge associated with each potential step was obtained by integrating the current-time (*i-t*) response after correcting for the background current signal. For $M(OH)_x$ (M = Ni, Co, Mn, Cr, Cu) catalysts, the pulse voltammetry process corresponds to the reversible transition between low-valence and high-valence metal ions. During the high-potential pulse, the catalyst undergoes oxidation via deprotonation, converting low-valence metal ions to high-valence states and resulting in the accumulation of oxidative charge on the catalyst surface. Upon applying the low potential, the catalyst reverts to its initial low-valence state. The quantity of high-valence metal ions generated during the test was determined by integrating the discharge region of the *i-t* curve. From this, the accumulated oxidative charge (corresponding to high-valence ions) at different potentials could be quantified. By plotting the accumulated oxidative charge as a function of potential, the deprotonation capability of the catalyst was evaluated.

Double-segment amperometric *i-t* tests

Double-segment amperometric *i-t* tests were performed to investigate the spontaneous chemical reaction between the main active intermediate (Ni(III)−OOH) and HMF during the

HMFOR process, which are referred to as broken-connection-pulse (BCP) tests. Each complete BCP test comprised an open-circuit period (400 s) followed by two segments of current-time (*i-t*) measurements under different applied potentials: a high potential of 1.52 V vs. RHE for 300 s and a low potential of 1.22 V vs. RHE for 300 s. The BCP procedures were carried out on different catalysts in three distinct electrolyte configurations: (i) 1 M KOH solution (KOH-test, (ii) 1 M KOH containing 50 mM HMF (HMFOR-test) and (iii) a sequential configuration in which the catalyst was first tested in 1 M KOH and then transferred to 1 M KOH with 50 mM HMF (KOH-HMFOR-test). In the KOH-HMFOR-test procedure, the first amperometric *i-t* segment at high potential was recorded in 1 M KOH for 300 s. The catalyst was subsequently transferred to 1 M KOH with 50 mM HMF, where an broken-circuit interval of 400 s was applied, followed by the second amperometric *i-t* segment at low potential for 300 s.

Optimized KOH-HMFOR-test

Optimized KOH-HMFOR-test were conducted to quantitatively evaluate the reaction kinetics between HMF and the main active intermediate (Ni(III)−OOH). In this procedure, the catalysts were first fully charged by performing an amperometric *i-t* test at a high potential of 1.52 V vs. RHE in 1 M KOH solution, ensuring complete oxidation of low-valence metal ions to their high-valence states. Subsequently, the fully charged catalysts were immersed in a 1 M KOH solution containing 50 mM HMF under broken-circuit conditions for varying durations, during which a redox reaction occurs between Ni(III)−OOH and HMF. The soaked catalysts were then promptly washed with ultrapure water to remove residual HMF from the surface. Finally, the discharge behavior of the washed catalysts was recorded in fresh 1 M KOH solution via a second amperometric *i-t* test at a low potential of 1.22 V vs. RHE. The discharge charge was obtained by integrating the current-time response after subtracting the background current, representing the amount of residual Ni(III)−OOH on the catalyst surface. The rate of the spontaneous chemical reaction during HMFOR was assessed by plotting the normalized charge ratio Q_t/Q_0 against immersion time t, where Q_t and Q_0 denote the discharge charge after soaking for time t and 0 s, respectively. The reaction kinetics were further analyzed using a first-order

kinetic model, expressed as: $\ln(Q_t/Q_0) = -kt$ where k is the first-order rate constant, reflecting the intrinsic reaction rate.

DFT information

DFT calculation method

All calculations were performed using the Vienna Ab-initio Simulation Package (VASP)[1,2]. The Perdew-Burke-Ernzerhof (PBE) functional within the generalized gradient approximation (GGA) was employed to describe the exchange-correlation interactions[3]. The projector augmented wave (PAW) method was used to treat the core-valence interactions, with a plane-wave cutoff energy of 400 eV. The DFT-D3 dispersion correction was included to account for van der Waals interactions. For structural optimization and static self-consistent calculations, a Monkhorst-Pack k-point mesh of 2 × 2 × 1 was used for density of states (DOS) calculations. Spin-polarized calculations were performed for all systems. The convergence criteria for electronic self-consistency and ionic relaxation were set to 1×10^{-5} eV and 0.02 eV/Å, respectively. All atoms were allowed to relax freely to their equilibrium positions. The pristine $Ni(OH)_2$ model was constructed based on the hexagonal $Ni(OH)_2$ structure. The bulk model with a 2 × 5 supercell was adopted, consisting of eight atomic layers of $Ni(OH)_2$. Three models (NiCoMn-LHs, NiCoMnCr-LHs and NiCoMnCrCu-LHs) were constructed by substituting Ni atoms with Co/Mn, Co/Mn/Cr, and Co/Mn/Cr/Cu heteroatoms respectively. All structures were fully optimized under the same computational parameters as the pristine model to obtain their ground-state geometries.

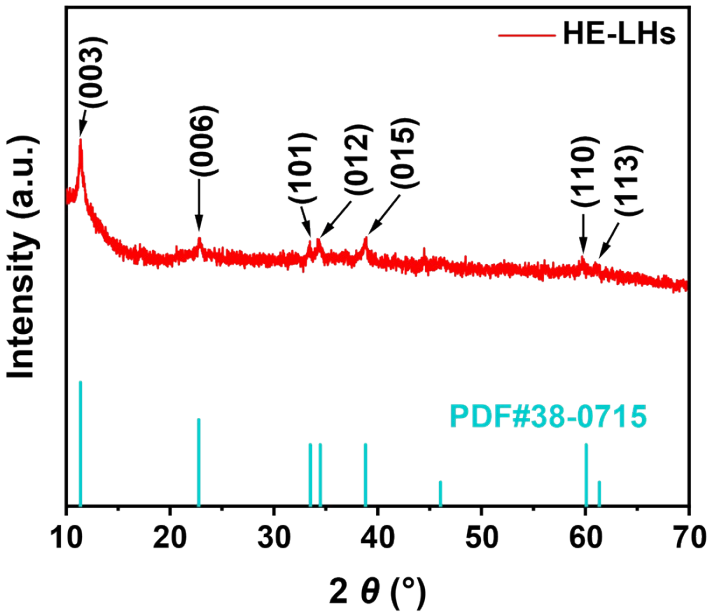

Figure S1. Enlarged XRD pattern of HE-LHs with JCPDS No. 38-0715 reference bars.

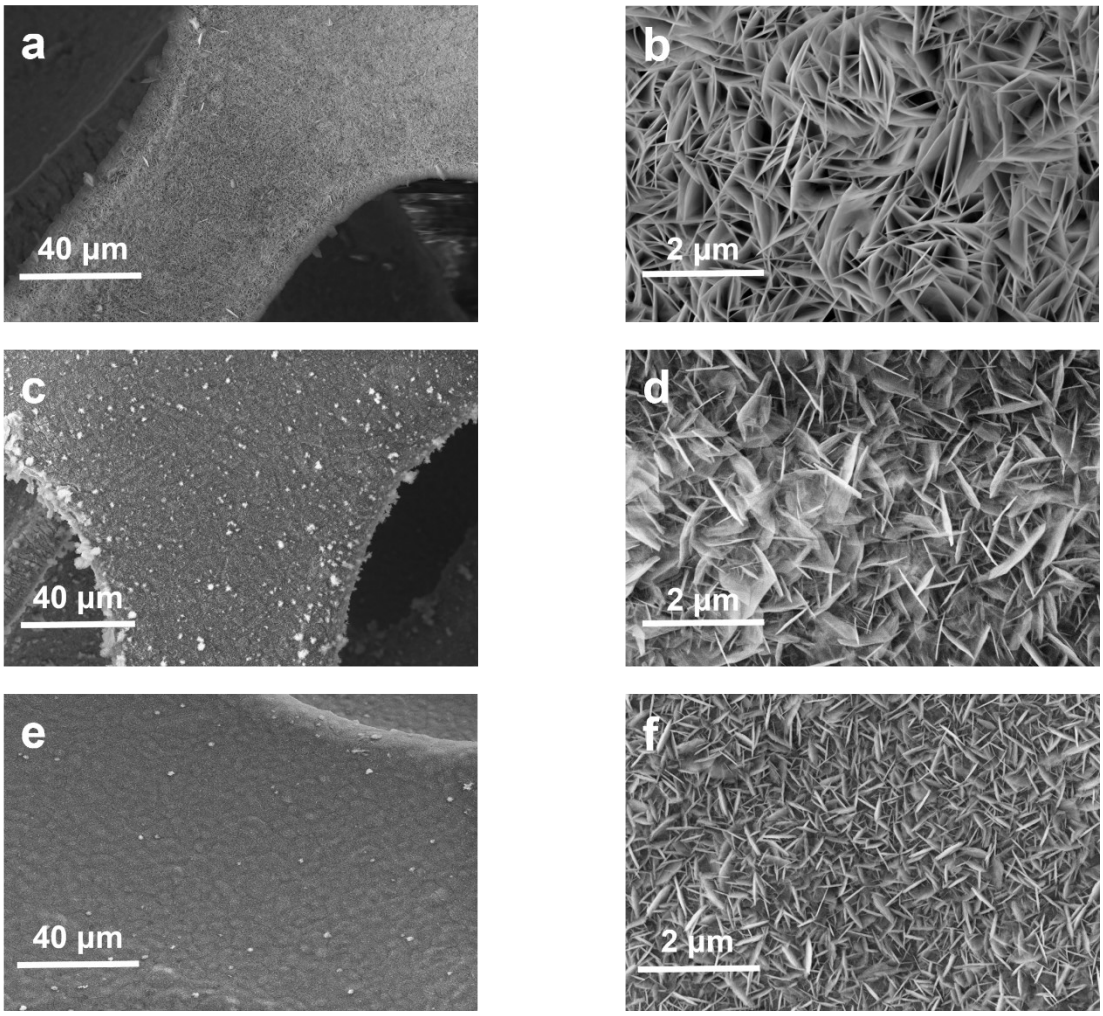

Figure S2. SEM images of (a-b) NiCoMn-LHs, (c-d) NiCoMnCr-LHs and (e-f) HE-LHs.

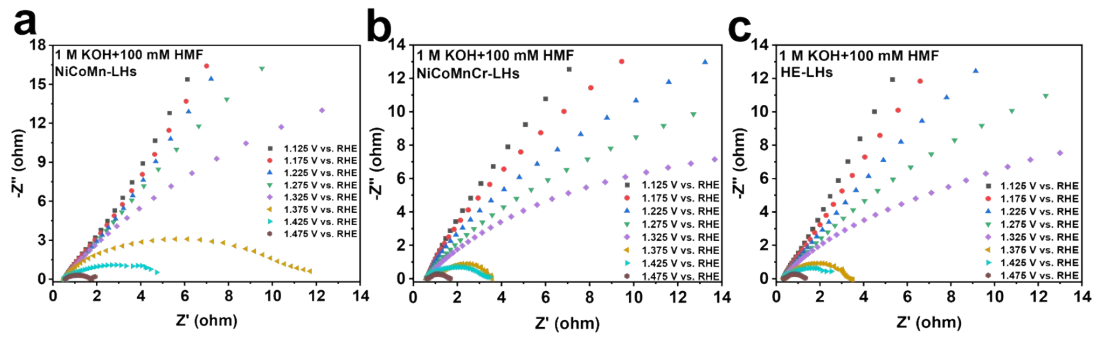

Figure S3. Nyquist plots in 1 M KOH with 100 mM HMF of (a) NiCoMn-LHs, (b) NiCoMnCr-LHs and (c) HE-LHs.

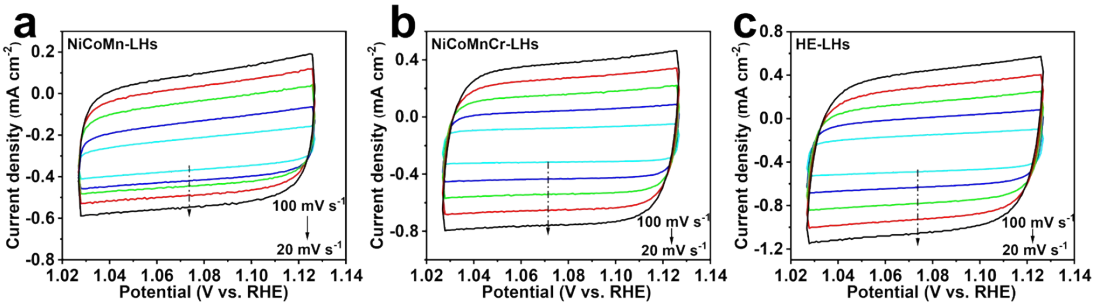

Figure S4. Cyclic voltammetry curves of (a) NiCoMn-LHs, (b) NiCoMnCr-LHs and (c) HE-LHs at different scan rates (20-100 mV s^{-1}) in 1 M KOH solution.

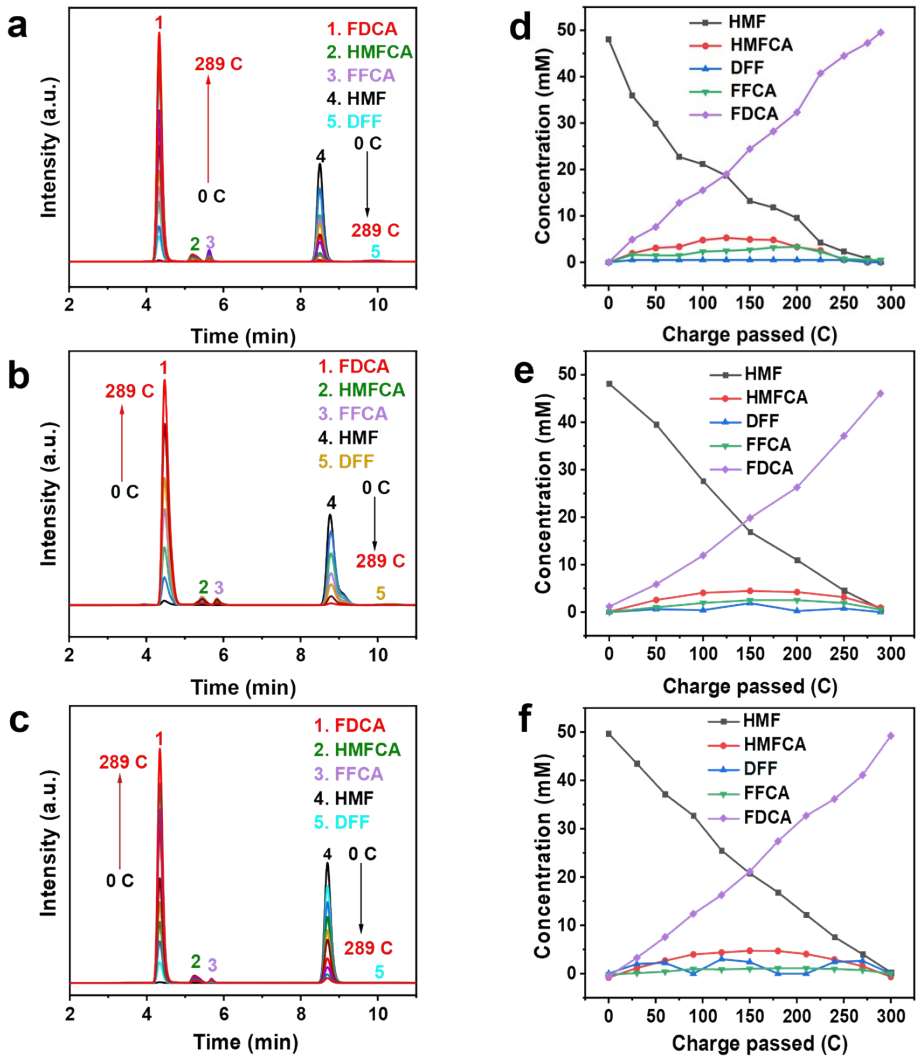

Figure S5. (a-c) Three independent replicate HPLC spectra at different charge intervals during the HMFOR at 1.475 V vs. RHE. (d-f) The corresponding change of HMF, HMFCA, DFF, FFCA and FDCA concentrations calculated from the HPLC data.

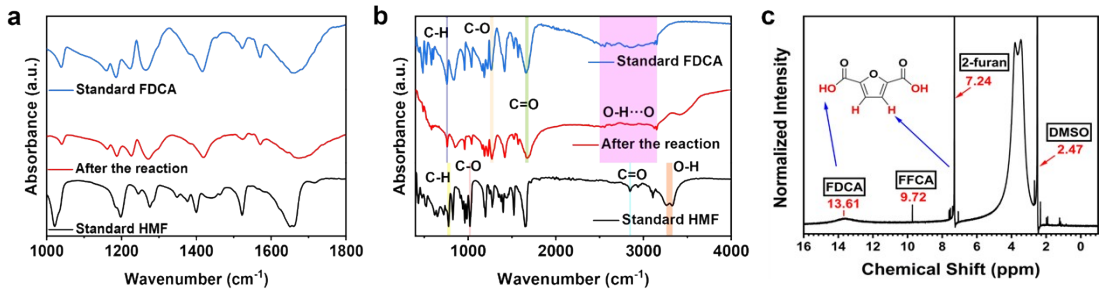

Figure S6. (a-b) FTIR spectra of as-collected product after reaction, standard FDCA and HMF. (c) ^{1}H NMR of as-collected product after reaction. After the electrocatalytic reaction, the electrolyte was acidified to pH=2 using dilute HCl to protonate the carboxylate groups (−COO^{-} to −COOH), followed by extraction with ethyl acetate and solvent evaporation to collect the solid product. The obtained white powder was then characterized by FTIR and NMR. In FTIR spectra, the product exhibits the characteristic broad, jagged O−H absorption of carboxylic acid dimers in the 2500-3500 cm^{-1} region, which is different from the broad peak at about 3300 cm^{-1} of alcohol O−H in HMF. Additionally, the aldehyde C−H stretch (2850 cm^{-1}) of HMF is absent. Moreover, the peaks of C=O in as-collected product and standard FDCA exhibit a higher wavenumber compared to that of HMF. This is because the conjugated aldehyde generally leads to a decrease in the wavenumber. The ^{1}H NMR spectrum of the as-collected product exhibits a chemical shift at 7.24 ppm ascribed to proton resonance from furan ring. And the weak and broad peak observed at 13.61 ppm is the proton resonance associated with the active carboxylic acid.

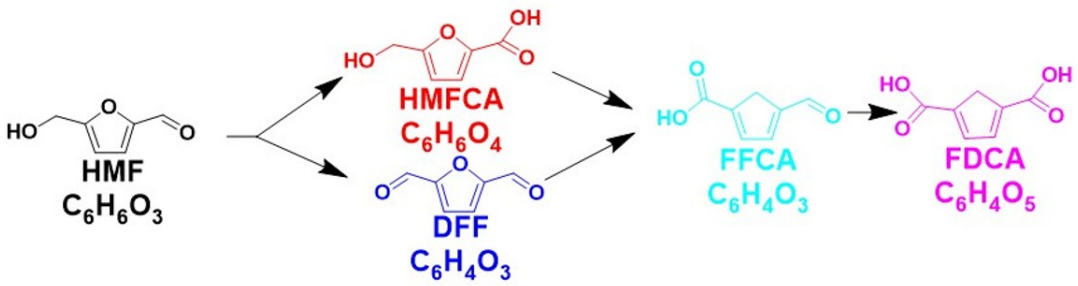

Figure S7. Proposed reaction pathways for HMFOR.

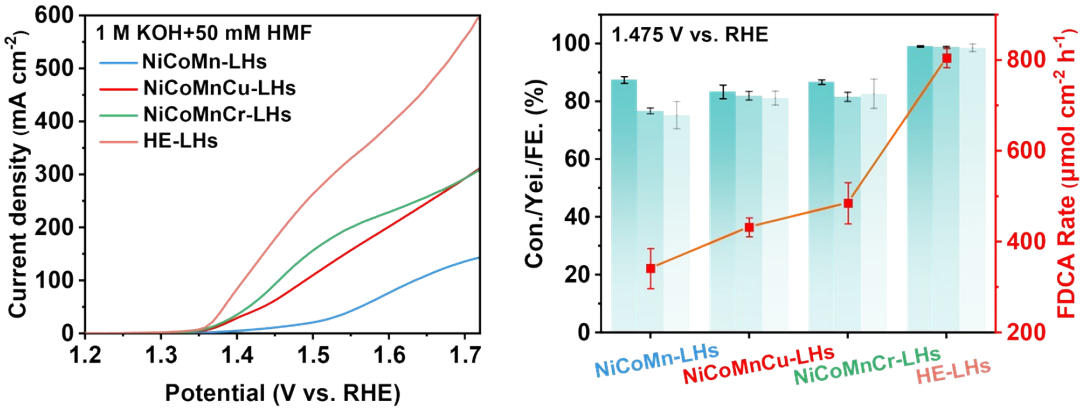

Figure S8. (a) LSV curves of NiCoMn-LHs, NiCoMnCu-LHs, NiCoMnCr-LHs and HE-LHs for HMFOR in 1 M KOH with 50 mM HMF. (b) HMF conversion, FDCA yield, FDCA FE and FDCA production rate of the LHs at 1.475 V vs. RHE.

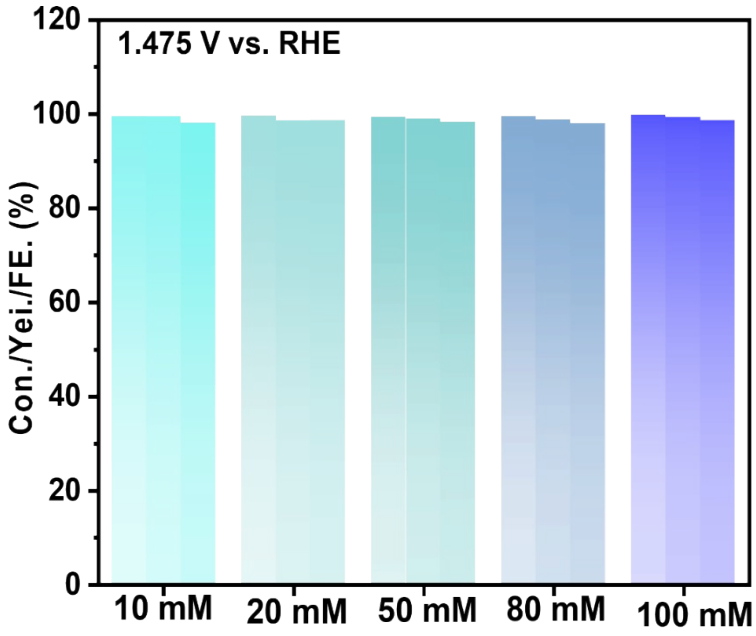

Figure S9. The HMF conversion, FDCA yield, and FDCA Faraday efficiency obtained from electrolysis of HMF at different concentrations under 1.475 V vs. RHE.

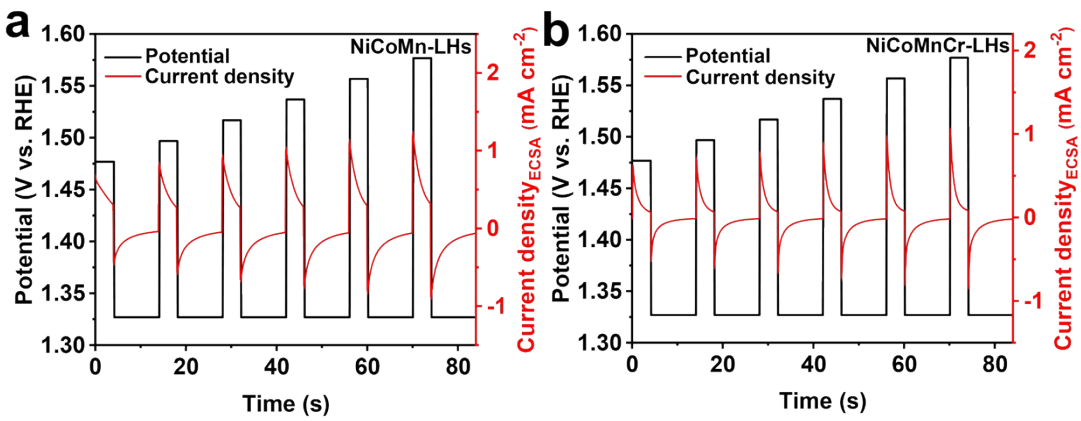

Figure S10. (a) NiCoMn-LHs and (b) NiCoMnCr-LHs of pulse voltammetry protocol between 1.32 V vs. RHE (low potential) and 1.47 V vs. RHE to 1.57 V vs. RHE (high potential) without iR-corrected potentials. The increased potential per step (Incr E) is 20 mV.

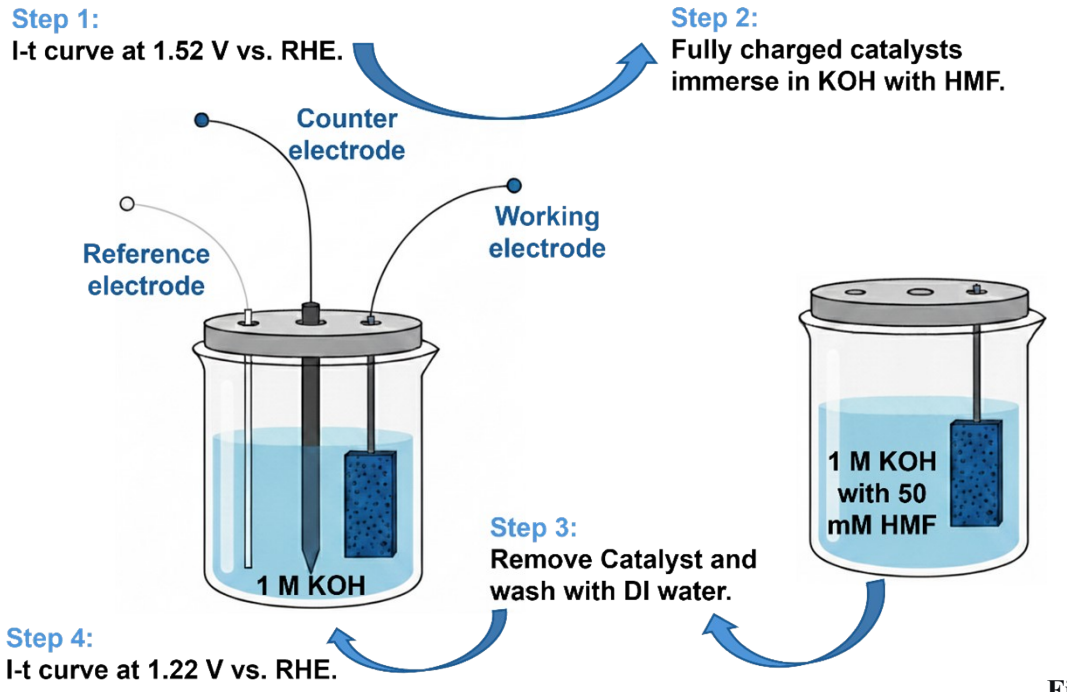

Figure S11. The schematic illustration of the optimized KOH-HMFOR test.

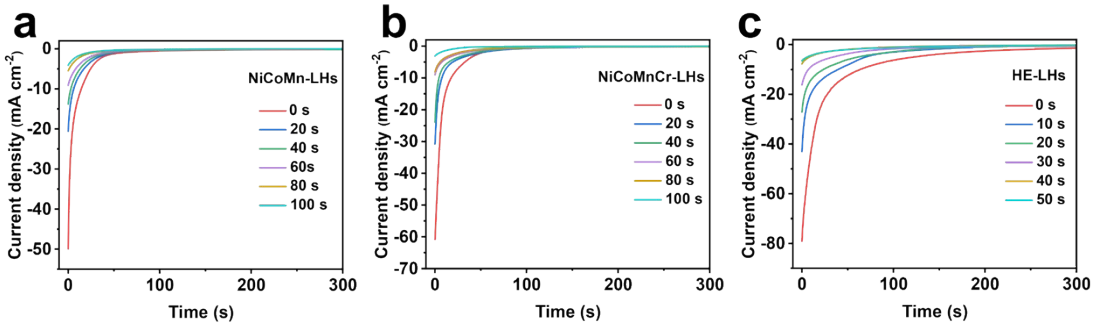

Figure S12. Discharge current curves of (a) NiCoMn-LHs, (b) NiCoMnCr-LHs and (c) HE-LHs in the 1 M KOH solution at low potential (1.22 V vs. RHE).

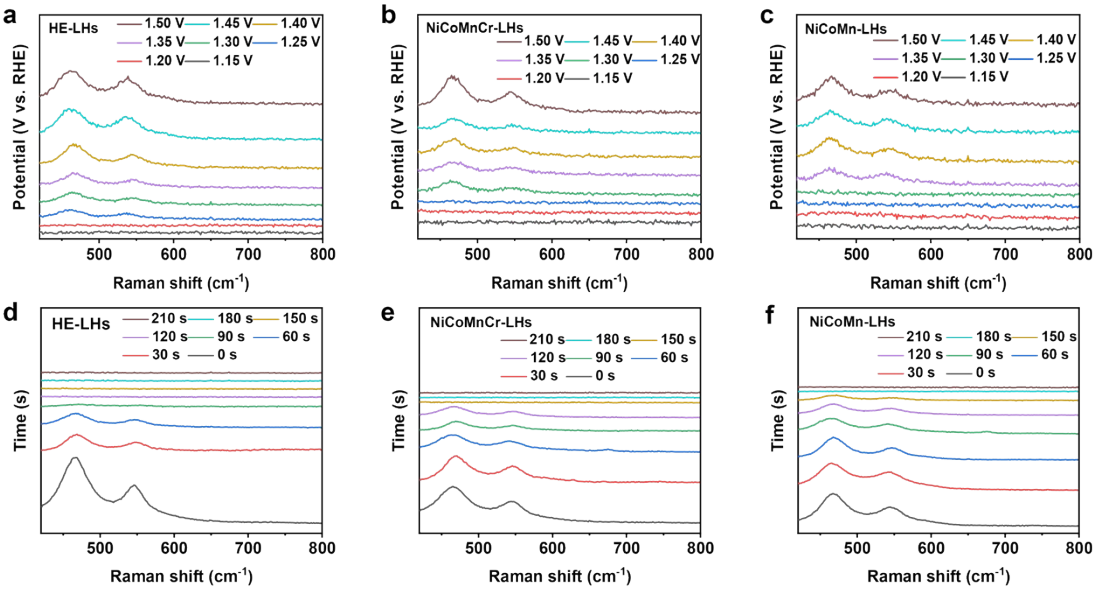

Figure S13. Dynamic evolution of the electrocatalysts. *In-situ* Raman spectra of (a) HE-LHs, (b) NiCoMnCr-LHs and (c) NiCoMn-LHs recorded with increasing potential. *In-situ* Raman spectra of (d) HE-LHs, (e) NiCoMnCr-LHs and (f) NiCoMn-LHs recorded with prolonging time (0-210 s) under break circuit potential.

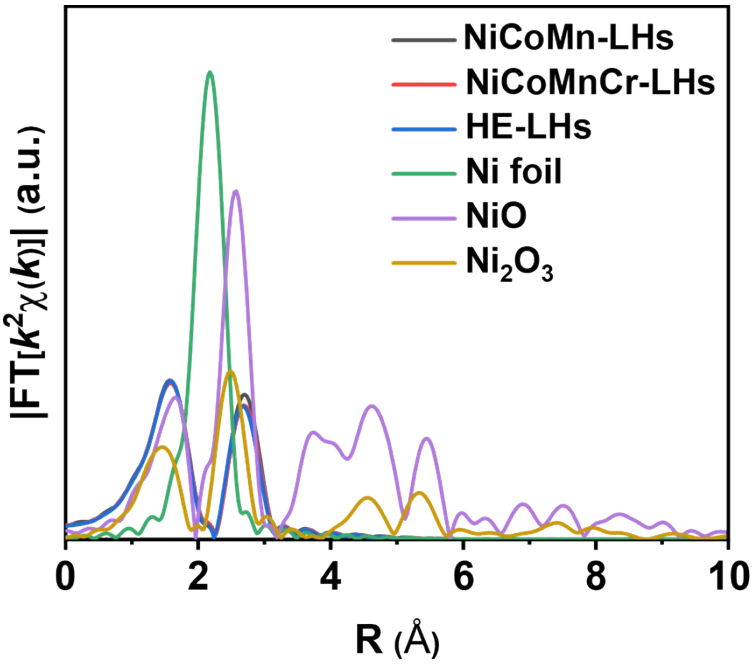

Figure S14. FT-EXAFS profiles of NiCoMn-LHs, NiCoMnCr-LHs, HE-LHs, Ni foil, NiO and Ni_2O_3.

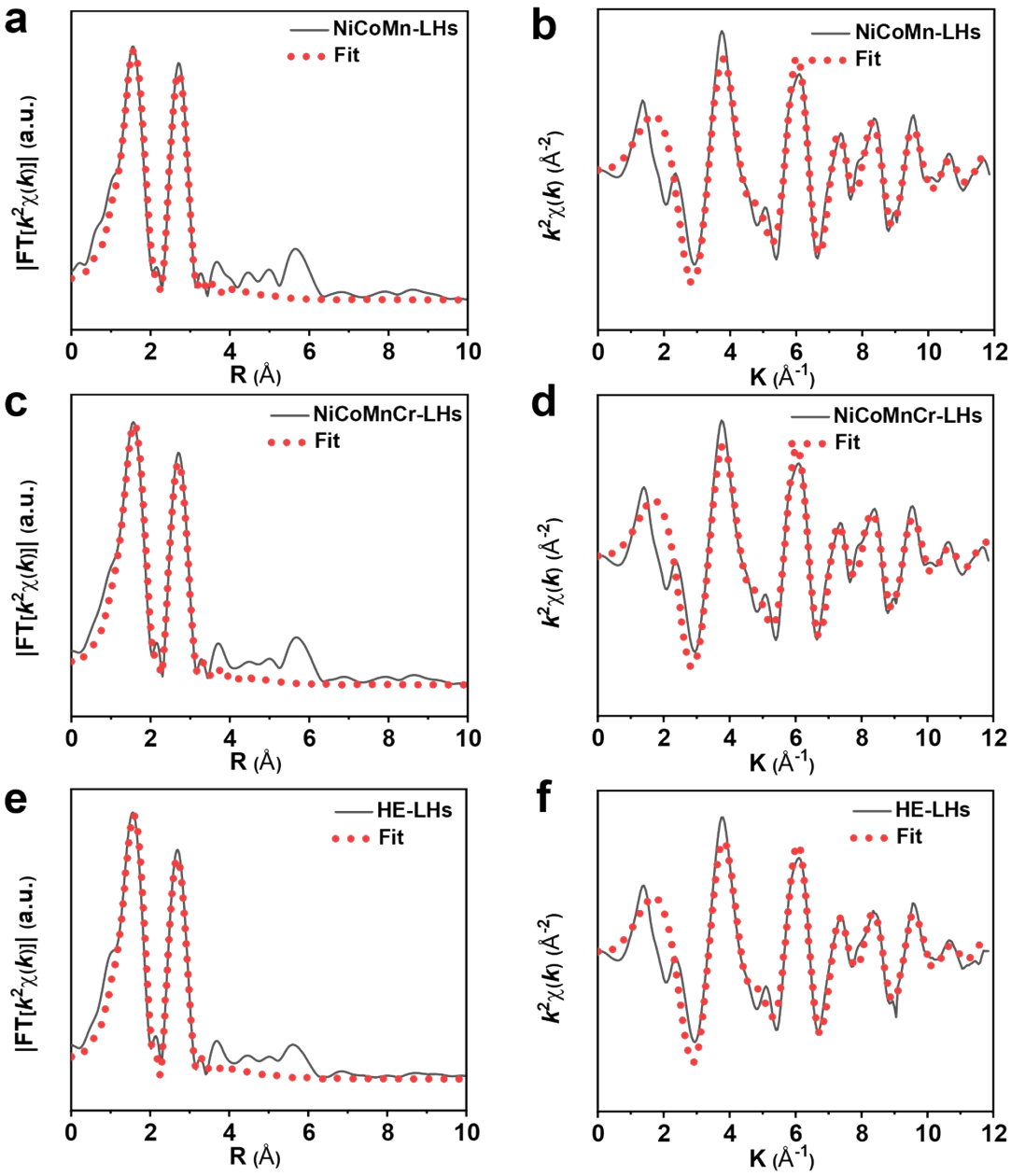

Figure S15. Ni *K*-edge EXAFS spectra and the Fourier-transformed magnitudes of (a-b) NiCoMn-LHs, (c-d) NiCoMnCr-LHs and (e-f) HE-LHs.

Table S1. The performance comparison for HE-LHs and other reported catalysts.

Catalysis	HMF concentration (mM)	*j* (mA cm^{-2}) /E_{RHE} (V)	HMF Conversion (%)	FDCA yield (%)	FDCA FE (%)	Ref.
NiCoFeMnAl-LDH	10	10/1.35	100	99.06	96.9	4
Pt/HEO	10	80/1.38	-	-	99.8	5
CC@LHA(7)	20	100/1.42	100	99.99	99.05	6
$Ni(OH)_2$-TPA	100	850/1.55	-	-	97.7	7
CC@NiFeCe(3%)-LDH	50	10/1.39	95.73	93.31	99.47	8
NiFe Alloys	10	10/1.35	97.2	86.6	94.2	9
Ni_3S_2/NiOx-15	20	366/1.5	-	-	98	10
GNPCH-900	10	10/1.37	-	-	90	11
CuCoNi	20	100/1.43	100	95.24	95.23	12
$Mo_{0.10}$-NiO	10	50/1.39	99.8	98.5	98.3	13
SC-MHEO	10	10/1.43	99.3	-	97.7	14
HE-LHs	50	10/1.331 50/1.38 100/1.41	99.4	99.0	98.4	This work

Table S2. EXAFS fitting results for the as-synthesized LHs at Ni-*K* edge.

Sample	**Shell**	**CN**	**R(Å)**	**σ2($Å^2$)**	**ΔE_0(eV)**	**K-range/ $Å^{-1}$**	**R-range/ Å**	**R factor**
NiCoMn-LHs	Ni-O	5.6±0.5	2.07±0.01	0.0081	-2.3±1.3	3.0-11.3	1.0-3.0	0.0119
	Ni-M	5.7±0.8	3.09±0.01	0.0089				
NiCoMnCr-LHs	Ni-O	5.4±0.5	2.06±0.01	0.0081	-2.6±1.4	3.0-10.9	1.0-3.0	0.0117
	Ni-M	5.5±0.6	3.08±0.01	0.0090				
HE-LHs	Ni-O	5.3±0.4	2.04±0.01	0.0082	-2.5±1.3	3.0-11.0	1.0-3.0	0.0121
	Ni-M	5.4±0.9	3.10±0.01	0.0089				

CN: coordination numbers; *R*: bond distance; σ^2: Debye-Waller factors; ΔE_0: the inner potential correction. *R* factor: goodness of fit. (S_0^2=0.78)

References

1 G. Kresse, J. Furthmüller, Efficient iterative schemes for ab initio total-energy calculations using a plane-wave basis set, *Phys. Rev. B Condens matter.*,1996, **54**, 11169-11186. https://doi.org/10.1103/PhysRevB.54.11169.

2 G. Kresse, D. Joubert, From ultrasoft pseudopotentials to the projector augmented-wave method, *Phys. Rev. B.*, 1999, **59**, 1758-1775. https://doi.org/10.1103/PhysRevB.59.1758.

3 J. P. Perdew, K. Burke, M. Ernzerhof, Generalized gradient approximation made simple, *Phys. Rev. Lett.*, 1996, **77** , 3865-3868. https://doi.org/10.1103/physrevlett.77.3865.

4 G. Ding, J. Zhang, D. Yan, Y. Yu, S. Li, L. Chen and G. Liao, High-entropy regulation of lattice oxygen p-band toward sustainable electrocatalytic biomass valorization, *Nano Lett*., 2025, **25**, 8984−8992.

5 G. Ding, Y. Yu, D. Yan, J. Zhang, S. L, L. Chen and G. Liao, Pt-activated surface nucleophilicity on high-entropy oxides enables superior biomass upgrading, *Adv. Funct. Mater*., 2026, **36**, e19698.

6 Y. Xin, H. Fu, L. Chen, Y. Ji, Y. Li and K. Shen, High-entropy engineering in hollow layered hydroxide arrays to boost 5-hydroxymethylfurfural electrooxidation by suppressing oxygen evolution, *ACS Cent. Sci*., 2024, **10**, 1920-1932.

7 D. Chen, W. Li, J. Liu and L. Sun, Bio-inspired proton relay for promoting continuous 5-hydroxymethylfurfural electrooxidation in a flowing system, *Energy Environ. Sci*., 2025, **18**, 3120-3128.

8 Y. Zhang, G. Hai, Z. Huang, Z. Liu, X. Huang and G. Wang, Ce-doping rather than CeO_2 modification and their synergistic effect: promotion from Ce species in the electrocatalytic oxidation of 5-hydroxymethylfurfural over NiFe–LDH, *Adv. Energy Mater*., 2024, **14**, 2401449.

9 L. Shi, W. Cai, F. Zhang, S. Li, X. Liu, Y. Liu, P. Ren, B. Li, S. Liu and B. Liu, Engineering oxygen intermediates adsorption on amorphous NiFe alloys for highly active and selective electrochemical biomass conversion, *Angew. Chem. Int. Ed*., 2025, **64**, e202424345.

10 D. Xiao, X. Bao, D. Dai, Y. Gao, S. Si, Z. Wang, Y. Liu, P. Wang, Z. Zheng, H. Cheng, Y. Dai and B. Huang, Boosting the electrochemical 5-hydroxymethylfurfural oxidation by balancing the competitive adsorption of organic and OH^- over controllable reconstructedNi_3S_2/NiO, *Adv. Mater*., 2023, **35**, 2304133.

11 C. Wang, Z. Zhao, W. Cao, Y. Peng, M. Song and Y. Wu, A metal-free carbonaceous material for highly efficient and robust electrochemical biomass valorization, *Adv. Funct. Mater*., 2025, **35**, 2502618.

12 W. Wang, F. Bai, K. Chu, M. Cai, X. Xu, Z. Guo, X. Zhang, J. Qin, Y. Huang and J. L. Song, Proton flux engineering via built-in electric fields in N-doped $CuO@Co_3O_4@Ni(OH)_2$ heterostructure for rechargeable Zn-NO_3^-/5-hydroxymethylfurfural multielectron transfer systems, *Angew. Chem. Int. Ed*., 2025, **64**,

e202514438.
13 Z. Sun, Z. Zhai, Z. Zheng, J. Chen, S. Yin, H. Wen, J. Wu and S. Yin, Hard lewis acid sites modulate competitive adsorption in nickel oxide for efficiency 5-hydroxymethylfurfural oxidation, *Adv*. *Funct*. *Mater*., 2025, **36**, e16593.
14 Y. Wang, H. He, H. Lv, F. Jia, and B. Liu, Two-dimensional single-crystalline mesoporous high-entropy oxide nanoplates for efficient electrochemical biomass upgrading, *Nat*. *Commun*., 2024, **15**, 6761.